

Structural properties and anisotropic electronic transport in (110) SrIrO₃ films

K. R. Kleindienst¹, K. Wolff¹, J. Schubert^{2,3}, R. Schneider¹, and D. Fuchs¹

¹Karlsruher Institut für Technologie, Institut für Festkörperphysik, 76021 Karlsruhe, Germany

²Forschungszentrum Jülich, Peter Grünberg Institut (PGI-9), 52425 Jülich, Germany

³JARA-FIT - Jülich-Aachen Research Alliance for Fundamentals of Future Information Technology,
Forschungszentrum Jülich GmbH, 52425 Jülich, Germany

ABSTRACT

Perovskite SrIrO₃ (SIO) films epitaxially grown on orthorhombic (110) GdScO₃ (GSO) and DyScO₃ (DSO) are found to display bulk-like orthorhombic structure with space group *Pbnm*. However, film deposition on cubic (001) SrTiO₃ or (LaAlO₃)_{0.3}(Sr₂AlTaO₆)_{0.35} (LSAT) induces a monoclinic distortion and twinned growth of SIO. Resistance measurements on the SIO films reveal only weak temperature dependence, where *R* increases with decreasing *T*, indicating the proximity to a metal-insulator transition. Hall measurements show dominant electron-like transport throughout the temperature range from 2 K to 300 K. At 2 K, the electron concentration and mobility amount to $n_e = 1.4 \times 10^{20} \text{ cm}^{-3}$ and 205 cm²/(Vs). Interestingly, the film resistance for the two orthogonal directions along the substrate edges of GSO and DSO is not the same and differs by up to 25% indicating pronounced anisotropic behavior with a specific *T*-dependence. The experimental results show that structural changes of the substrate material are likely responsible for the observed anisotropic electronic transport. The substrate-induced effects are likely related to constraints with respect to IrO₆ octahedral rotations. The strong sensitivity of the electronic transport in SIO films to substrate-induced structural changes may be explained in terms of the narrow electron-like bands in SIO caused by spin-orbit-coupling and orthorhombic distortion.

I. INTRODUCTION

The strong spin-orbit-coupling (SOC) in 5*d* iridium-based transition-metal oxides results in comparable energy scales of the electron correlation, electronic bandwidth, and SOC [1,2], which makes these materials promising candidates for the emergence of new topological phenomena or quantum states [3-7]. Systematic dimension-controlled physical properties are observed in the Ruddlesden-Popper series Sr_{*n*+1}Ir_{*n*}O_{3*n*+1} (*n* = 1, 2, and ∞) [8]. In Sr₂IrO₄ (*n* = 1) the crystal-field splitting and SOC lead to new spin-orbital mixed states. The five 5*d* electrons of Ir⁴⁺ result in a filled low-energy J_{eff} = 3/2 quartet band and a half-filled high-energy J_{eff} = 1/2 doublet band. Moderate Coulomb interaction opens a Mott-gap which leads to an antiferromagnetic insulating ground state with J_{eff} = 1/2 [9]. In the perovskite SrIrO₃ (SIO) (*n* = ∞), the network of corner-

shared IrO_6 octahedra provides a better hybridization between Ir $5d$ orbitals and O $2p$ -orbitals that favors a paramagnetic semi-metallic ground state [10,11]. Tilts and rotations of the relatively rigid IrO_6 octahedra, i. e., an in-phase rotation along the c -axis and anti-phase rotations along the a - and b -axes, cause an enlargement of the perovskite unit cell by $\sqrt{2}\times\sqrt{2}\times 2$ with an, according to the Glazer notation [12], $a^-a^-c^+$ octahedral tilt pattern and an orthorhombic structure with space group $Pbnm$ (62) [13].

However, the metastable form of SIO prevents single-crystal growth under ambient pressure, where only the monoclinic modification with $C2/2$ (15) dominates the ambient phase [14]. Nevertheless, SIO could be successfully synthesized in polycrystalline form under pressure ($p \approx 40$ kbar) [13-15] or be stabilized by the epitaxial growth of thin films [16-20]. Therefore, epitaxially grown SIO films are of current interest to explore the system. In addition, SIO films might act as a key building block for engineering topological phases at interfaces and in heterostructures [21,22].

Despite the larger coordination and dimensionality compared to the quasi two-dimensional insulating counterpart Sr_2IrO_4 , the electronic bandwidths of SIO are found to be narrower displaying a semi-metallic electronic structure. In particular, its Fermi surface consists of multiple heavy hole- and light electron-like bands. The 2 – 6 times lighter quasiparticle mass of the electrons allows them to dominate electronic transport explaining the commonly observed electron-like single-type carrier transport in SIO [19, 20,23]. Very recently it was shown that in SIO thin films the electronic structure is controlled by a subtle interplay between octahedral rotations, SOC, and dimensionality [11,24,25]. This paves the way for a distinct tuneability of the physical properties by epitaxial strain and film thickness. For example, angle resolved photoemission spectroscopy (ARPES) and first-principle calculations [11] show that substantial changes in the electronic structure and the physical properties of SIO are achieved by subtle changes in the structure and rotation angles of the IrO_6 octahedra. For SIO films on SrTiO_3 (STO) substrates bulk-like electronic structure is observed for a film thickness $t > 9$ unit cells (3.2 nm), i. e., paramagnetic metallic behavior with a partially filled $J_{\text{eff}} = 1/2$ band. In contrast, for $t \leq 3$ unit cells a distinct charge gap opens leading to a metal-insulator transition, which on a first glance appears to be in analogy to the dimensional driven metal-insulator transition in the Ruddlesden Popper iridates with decreasing n [24,25]. However, the gap-opening is accompanied by a structural transition and thus very likely not caused by the decreased film thickness alone. Specifically, a suppression of in-plane rotations of the IrO_6 octahedra is observed which has been discussed in terms of constraints upon octahedral in-plane rotations imposed by the cubic STO substrate.

In this paper, we demonstrate and discuss anisotropic electronic transport of SIO films epitaxially grown on various substrate materials. The structural properties, especially orthorhombic distortion, were characterized in detail. Anisotropic electronic transport was found for (110) oriented SIO films on (110) DyScO_3 (DSO) and (110) GdScO_3 (GSO) substrates. The distinct T -dependence of the resistance anisotropy hints to a substrate-induced effect and indicates a high

sensitivity of the electronic transport in SIO to structural distortions. The narrow multiple band structure caused by the orthorhombic distortion and SOC in combination with the semi-metallic behavior of SIO may be the reason for that.

II. EXPERIMENTAL

Epitaxial perovskite SrIrO₃ (SIO) films were grown by pulsed laser deposition using home-made single-phase (monoclinic) polycrystalline SrIrO₃ targets that were prepared by standard solid-state sintering under ambient pressure. The laser ablation results in a sizeable non-stoichiometric redeposit of ablated materials on the target surface. For this reason, targets were re-polished before each film deposition. The films were deposited at a substrate temperature $T_s = 700^\circ\text{C}$. The thermodynamic stability of neighbored phases of the Ruddlesden-Popper series, i. e., Sr₂IrO₄ and Sr₃Ir₂O₇ and the large volatility of Ir-oxide species generate a large sensitivity of the Sr/Ir ratio in the film with respect to the deposition parameters, even though single phase targets of SrIrO₃ are used [26,27]. Chemical film composition was checked by Rutherford backscattering spectrometry (RBS) using He⁺ ions with an energy of 1.4 MeV. The computer software RUMP provided the numerical analysis of the RBS-data [28].

A linear dependence of the Sr/Ir ratio was found for laser fluence $0.7 \text{ J/cm}^2 \leq F \leq 1.1 \text{ J/cm}^2$ and an oxygen partial pressure $0.01 \text{ mbar} \leq p(\text{O}_2) \leq 0.1 \text{ mbar}$, see Fig. 1. This in turn allows a precise control of the chemical composition. Stoichiometric conditions are obtained for $p(\text{O}_2) \approx 0.1 \text{ mbar}$ and $F \approx 1 \text{ J/cm}^2$. The deposition rate amounts to about 0.1 \AA per laser pulse. To provide additional oxygenation, the films were cooled down in $p(\text{O}_2) = 0.5 \text{ bar}$.

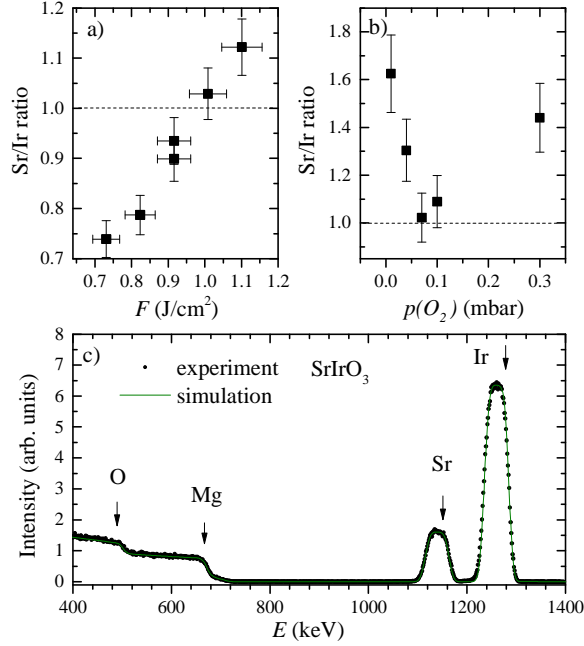


FIG. 1. (a) Sr/Ir ratio of deposited films versus laser fluence F for $p(\text{O}_2) = 0.1$ mbar and (b) versus $p(\text{O}_2)$ for $F = 1$ J/cm². The Sr/Ir ratio was determined by Rutherford backscattering spectrometry (RBS). Error bars are calculated from standard deviations by measuring multiple samples of each type. Dashed lines indicate stoichiometric composition. (c) RBS spectrum (full circles) for film deposited at $p(\text{O}_2) = 0.1$ mbar and $F = 1$ J/cm² on a MgO substrate. The chemical elements corresponding to the peaks are indicated. A fit to the spectrum is shown by the solid line that reveals stoichiometric composition of SrIrO₃.

Epitaxial SIO films were grown on different substrate materials, i. e., (110) oriented GdScO₃ (GSO), (110) DyScO₃ (DSO), (001) SrTiO₃ (STO), (001) (LaAlO₃)_{0.3}(Sr₂AlTaO₆)_{0.35} (LSAT), and (110) NdGaO₃ (NGO). Table I summarizes structural parameters and surface orientation of the substrate materials. To compare structural properties of the films that were grown under different epitaxial strain conditions the film thickness was kept constant at $t \approx 60$ nm.

TABLE I. Space group (SG), crystallographic orientation (CO) of the surface normal, lattice parameters a , b , and c , orthorhombic distortion ($a/b-1$), pseudo-cubic lattice parameter a_{pc} of bulk SrIrO₃ (SIO) [13] and the used substrate materials. In addition, the corresponding lattice mismatch $\Delta = (a_{\text{pc}}(\text{sub}) - a_{\text{pc}}(\text{SIO}))/a_{\text{pc}}(\text{SIO})$ with respect to bulk SrIrO₃ is noted down. For the orthorhombic substrates a_{pc} is deduced from the orthorhombic lattice spacing d_{220} and d_{002} , i. e., $a_{\text{pc}} = (d_{220}^2 + d_{002}^2)^{1/2}$. Here, LSAT is (LaAlO₃)_{0.3}(Sr₂AlTaO₆)_{0.35}.

	SG	CO	a (Å)	b (Å)	c (Å)	$(a/b-1)(\%)$	a_{pc} (Å)	Δ (%)
SrIrO ₃	<i>Pbnm</i>		5.6	5.57	7.89	+0.52	3.959	0
GdScO ₃	<i>Pbnm</i>	110	5.48	5.75	7.93	-4.7	3.969	+0.22
DyScO ₃	<i>Pbnm</i>	110	5.44	5.72	7.91	-4.1	3.950	-0.22
SrTiO ₃	<i>Pm-3m</i>	001	3.905	3.905	3.905	0	3.905	-1.36
LSAT	<i>Pm-3m</i>	001	3.874	3.874	3.874	0	3.874	-2.14
NdGaO ₃	<i>Pbnm</i>	110	5.43	5.5	7.71	-1.2	3.859	-2.52

Structural properties of the SIO films, such as film thickness, surface roughness, lattice parameters and symmetry, crystallinity, epitaxial growth and strain were characterized by x-ray diffraction experiments using a Bruker D8 Diffractometer equipped with CuK_α radiation ($\lambda = 1.5418 \text{ \AA}$) in reflectivity, diffraction and non-coplanar grazing incidence mode.

Electronic transport was probed by four-point resistance measurements in van der Pauw geometry using a physical property measuring system (PPMS) from Quantum Design. An alternating current excitation of $I_{\text{ac}} = 10 \text{ \mu A}$ was used. Electrical contacts for the measurements were made to the corners of the square-shaped sample surface ($5 \text{ mm} \times 5 \text{ mm}$) using ultrasonic Al-wire (diameter = 15 \mu m) bonding. In these conditions, the so called Montgomery method [29] is particularly sensitive to anisotropic electronic transport and therefore suitable to study electronic anisotropy in, e. g., orthorhombic materials [30]. To reduce the influence of possible surface degradation on SIO film resistance [20] the measurements were carried out shortly after film deposition. In addition, the films were prepared with a rather large film thickness ($t \approx 60 \text{ nm}$) to minimize surface effects.

III. RESULTS AND DISCUSSION

A. Structural and epitaxial properties of SrIrO_3 thin films

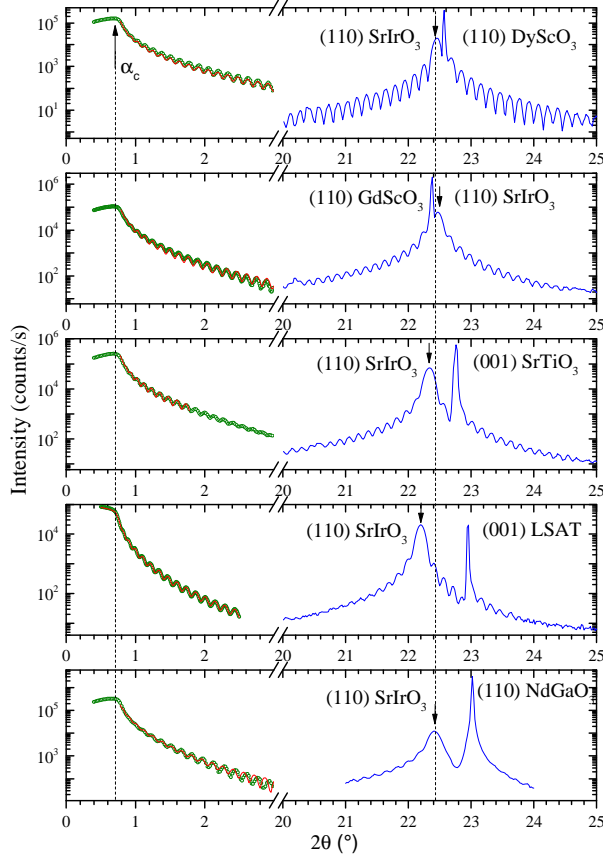


FIG. 2. X-ray reflectivity (left spectrum, green circles) and corresponding fit to the data (red line) of epitaxial SrIrO₃ thin films ($t \approx 60$ nm) deposited on various substrates. The critical angle of total reflection, α_c , is indicated by arrow and dashed line. Symmetric x-ray diffraction ($2\theta/\omega$ -scans) from lattice planes that are perpendicular to the surface normal (right spectrum). The central peak position of the film as indicated by arrow shows variation for the different substrate materials. The dashed line corresponds to the (110) peak position of bulk SrIrO₃.

In Fig. 2 we have shown the x-ray reflectivity and diffraction ($2\theta/\omega$ -scan) of epitaxial SIO films deposited with comparable thickness t on various substrate materials (see Table I). Reflectivity profiles yield a similar critical angle of total reflection at $\alpha_c \approx 0.73^\circ$ for all samples. From the best fits to the Kiessig fringes in the spectra above α_c we deduce a material density $D \approx 8.8$ g/cm³, the surface roughness $R_a \approx 5$ Å and the film thickness $t \approx 60$ nm [31]. The clear observation of Kiessig fringes and the rather low R_a already indicate good layer-by-layer growth mode of SIO. Structural parameters that are obtained from the fits are summarized in Table II.

Symmetric $2\theta/\omega$ -scans of the lattice planes that are perpendicular to the surface normal are shown up to the first order reflections on the right of Fig. 1. The central peak positions of the films are seemingly sensitive to the substrate. Beside line broadening of the central peak due to the finite film thickness the diffraction displays Laue oscillations caused by coherent scattering of lattice planes, well beyond to the left and right of the central peak position, documenting an

epitaxial layer-by-layer growth mode and a high crystalline quality of the films. With respect to the pseudo-cubic lattice parameter a_{pc} the sequence of unit-cell size is: $a_{pc}(\text{GSO}) > a_{pc}(\text{SIO}) > a_{pc}(\text{DSO}) > a_{pc}(\text{STO}) > a_{pc}(\text{LSAT}) > a_{pc}(\text{NGO})$, see Table I. Hence, with respect to the dashed line, indicating the (110) peak position of bulk SIO, substrate reflections are systematically shifted to the left ($a_{pc} > a_{pc}(\text{SIO})$) or to the right ($a_{pc} < a_{pc}(\text{SIO})$). SIO films on DSO display similar out-of-plane lattice spacing $d_{110} \approx a_{pc}(\text{SIO})$ due to the nearly perfect lattice matching $\Delta = (a_{pc}(\text{sub}) - a_{pc}(\text{SIO}))/a_{pc}(\text{SIO}) \approx -0.22\%$, where $a_{pc}(\text{sub})$ is the pseudo-cubic lattice parameter of the substrate material. Negative lattice mismatch suggests compressive in-plane strain on SIO. With decreasing $a_{pc}(\text{sub})$, compressive strain on SIO is expected to increase. However, SIO on NGO shows bulk like d_{110} lattice spacing again. The large lattice mismatch between SIO and NGO ($\Delta = -2.52\%$) very likely results in a fast structural relaxation and relieve of compressive lattice strain, indicating a small critical film thickness t_c above that structural relaxation sets in.

To determine in-plane lattice parameters and orthorhombic distortion extensive x-ray diffraction measurements were carried out on various asymmetric film reflections. In Fig. 3, we have plotted $2\theta/\omega$ scans on asymmetric reflections of SIO films on DSO (top), GSO (middle), and STO (bottom) to document orthorhombic structure and epitaxial relationship of SIO films. In Fig. 3 (top), the orthorhombic lattice parameters of DSO ($a < b < c$) result in the following lattice spacing: $d_{260} > d_{444} > d_{620}$. As a result, the (260) reflection appears at smallest and the (620) at largest 2θ value. The (444) and (44-4) reflection have the same lattice spacing and hence 2θ position. Orthorhombic distortion, i. e., $d_{260} \neq d_{620}$ is also verified for SIO. However, here we have $b < a < c$, similar to that of bulk SIO, see Table I. Furthermore, the orthorhombic distortion is obviously much smaller for SIO (0.34%) compared to DSO (-4.1%), see Tables I and II, resulting in a much smaller difference between the 2θ -values of the (260) and (620) reflection. However, with respect to the orthorhombic distortion of bulk SIO (+0.52%), the distortion of the SIO film is only slightly smaller. Comparing the orthorhombic distortion of SIO on DSO (0.34%) and SIO on GSO (+0.17) (Fig. 2, middle), a distinct reduction is observed for slightly tensile strained SIO film growth on GSO ($\Delta = +0.22\%$) compared to a more compressive growth on DSO ($\Delta = -0.22\%$). Hence, tensile strain seems to reduce orthorhombic distortion, which can be well understood in terms of unit-cell size. A larger lattice parameter allows for more straightening of the Ir-O-Ir bond angle towards 180° (less buckling of IrO_6 octahedra) thereby reducing octahedral tilts and orthorhombic distortion in case of regular IrO_6 octahedra. For SIO on STO (Fig. 2, bottom) orthorhombic distortion seems to be negligible ($a \approx b$).

The film lattice parameters are deduced from the (110), (220), (260), (444) and (620) reflections. Table II summarizes the lattice parameters and the related orthorhombic distortion of the SIO films.

TABLE II. Structural properties of epitaxial SrIrO₃ (SIO) films grown on various substrates. Film thickness t and surface roughness R_a are deduced from x-ray reflectivity measurements. Orthorhombic lattice parameters and distortion as well as the pseudo-cubic unit-cell volume $V_{pc} = (d_{220}^2 \times d_{002})$, where d_{220} and d_{002} are the orthorhombic lattice spacing, are obtained from x-ray diffraction. For bulk SIO $V_{pc} \approx 61.6 \text{ \AA}^3$.

SIO on:	t (nm)	R_a (Å)	a (Å)	b (Å)	c (Å)	$(a/b-1)(\%)$	V_{pc} (Å ³)
GSO	58	5	5.59	5.58	7.9	+0.17	61.6
DSO	58	5	5.61	5.59	7.92	+0.34	62
STO	60	5	5.58	5.58	7.82	0 #	60.8
LSAT	59	5	5.6	5.6	7.82	0 #	61.3
NGO	55	10	5.59	5.59	7.91	0 \$	61.7

#: SIO films on STO or LSAT display monoclinic distortion, i. e., $\gamma = 88.82^\circ$ and 87.54° , respectively. \$: Orthorhombic distortion might be invisible due to strong lattice relaxation.

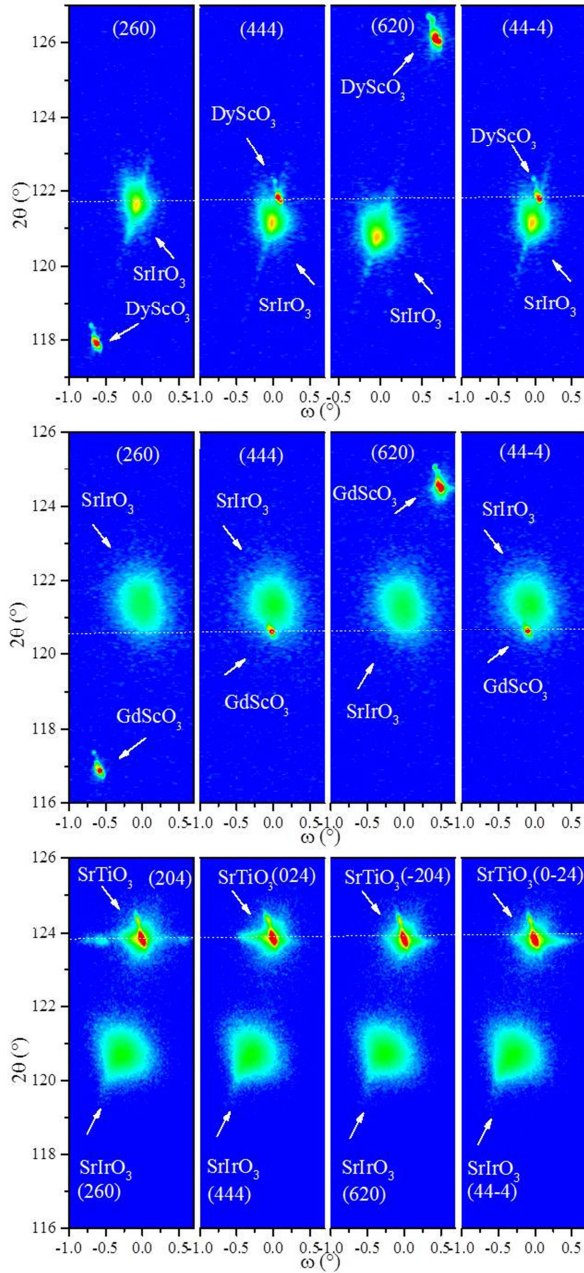


FIG. 3. $2\theta/\omega$ scans on asymmetric reflections of SrIrO_3 film on (110) DyScO_3 (DSO) (top), (110) GdScO_3 (GSO) (middle), and (001) SrTiO_3 (STO) (bottom). Reflections are noted with respect to orthorhombic structure. The contour plots display scattered intensity on a logarithmic scale as a function of the 2θ and ω value referring in case of DSO and GSO (STO) to the [110] ([001]) surface normal and from left to the right to the azimuth reference [-110] ([100]), [001] ([010]), [1-10] ([-100]), and [00-1] ([0-10]).

The octahedral tilt pattern, i. e., the rotation pattern of IrO_6 octahedra in the SIO film is found to be the same as those of DSO and bulk SIO. The appearance of specific orthorhombic reflections, i. e., the presence of half-integer Miller indices in case of a pseudo-cubic perovskite lattice,

confirms a cell doubling due to octahedral tilt or rotations. Due to the generally low intensity of such reflections, lab-source x-ray diffraction instruments are less suitable and experiments with synchrotron radiation are preferred. However, the high crystalline quality of these films allowed us to verify such reflections for the SIO films and to validate orthorhombic $a\bar{a}c^+$ tilt pattern and hence $Pbnm$ (62) symmetry, see APPENDIX.

SIO films that were deposited on cubic substrates with 4-fold in-plane symmetry, i. e., STO and LSAT, do not possess any sizable orthorhombic distortion ($a \approx b$), see Fig. 3 (bottom). Moreover a monoclinic distortion appears. The monoclinic distortion ($\alpha = \beta = 90^\circ$, $\gamma < 90^\circ$) likely helps compensate the lattice mismatch between the orthorhombic a/b -axes lattice parameter of SIO (a_{SIO}) and the cubic a -axis in-plane lattice parameter of STO or LSAT (a_c). We deduced the monoclinic distortion by $\sin(\gamma/2) = a_c/a_{\text{SIO}}$. Obviously, with increasing compressive lattice strain, i. e., decreasing a_c , monoclinic distortion increases from $\gamma = 88.82^\circ$ for SIO on STO to $\gamma = 87.54^\circ$ for SIO on LSAT, see Table II. Nevertheless, due to the four-fold in-plane symmetry of STO and LSAT, the corresponding SIO films are found to be twinned. This has been verified by the occurrence of specific (half-integer) film reflections, as detailed in the APPENDIX.

The epitaxial relationship of SIO with respect to the used substrate materials is summarized again in Table III.

TABLE III. Epitaxial relationship of SrIrO₃ films with respect to the single-crystal substrates used for the epitaxial growth. Substrate orientation with respect to the surface normal, i. e., out-of-plane orientation is given in the first column. Out-of-plane and in-plane lattice directions are given in the second and third column. SIO films are twinned when they are grown on STO or LSAT.

SIO on:	<i>out-of-plane orientation</i>	<i>in-plane orientation</i>
(110) GSO	SIO [110] parallel to GSO [110]	SIO [001] parallel to GSO [001]
(110) DSO	SIO [110] parallel to DSO [110]	SIO [001] parallel to DSO [001]
(001) STO	SIO [110] parallel to STO [001]	SIO [001] parallel to STO [010]/[100]
(001) LSAT	SIO [110] parallel to LSAT [001]	SIO [001] parallel to LSAT [010]/[100]
(110) NGO	SIO [110] parallel to NGO [110]	SIO [001] parallel to NGO [001]

Since the SIO films were grown on substrate materials displaying different lattice mismatch with respect to the crystal structure of bulk SIO, the films are likely epitaxially strained. Generally, lattice strain caused by lattice mismatch between film and substrate material is relieved and compensated during film growth by introducing defects or lattice distortions above a so-called critical film thickness t_{cr} resulting in a change of the lattice parameters with increasing film thickness for $t > t_{\text{cr}}$. In Table IV we have summarized the lattice strain of SIO films grown on the various substrate materials. Strain was deduced from the lattice parameters given in Tables I and II, and therefore has to be regarded rather as a mean lattice strain. On a first glance, the strain values listed in Table IV are rather small and do not show any systematic trend with decreasing

in-plane lattice parameters of the substrate, i. e., from GSO to NGO (from top to bottom of Table IV). This indicates a nearly strain relieved state of the films. Irrespective of the substrate, the b -axis seems to be under a small tensile strain. A sizeable compressive strain is only found for the c -axis for the films grown on STO or LSAT. Since a - and b -axis components are present in in-plane as well as in out-of-plane direction, frustration with respect to lattice strain may occur. That might be the reason for the relative small value and change of Δd_{220} with increasing compressive lattice mismatch. Apparently, the most part of lattice strain is comprised within the c -axis lattice parameter. Further studies on the epitaxial strain and related strain-relaxation are detailed in the APPENDIX.

TABLE IV. Epitaxial strain of SrIrO₃ (SIO) films grown on various substrates with respect to bulk SIO. Film thickness t was kept nearly constant for all the films ($t \approx 60$ nm). The strain $\Delta a = (a_f - a_b)/a_b$, $\Delta b = (b_f - b_b)/b_b$, $\Delta c = (c_f - c_b)/c_b$, $\Delta d_{220} = (d_{220f} - d_{220b})/d_{220b}$, and $\Delta V_{pc} = (V_{pcf} - V_{pcb})/V_{pcb}$ was calculated from the structural parameters of the SIO films $a_f, b_f, c_f, d_{220f} = 1/2 \times (a_f^2 + b_f^2)^{1/2}$, and V_{pcf} (see Table II) and bulk SIO $a_b, b_b, c_b, d_{220b} = 1/2 \times (a_b^2 + b_b^2)^{1/2}$, and V_{pcb} (see Table I). Positive or negative signs indicate tensile or compressive strain, respectively. The pseudo-cubic unit-cell volume $V_{pc} = (d_{220}^2 \times d_{002})$, where d_{220} and d_{002} are the orthorhombic lattice spacing. For bulk SIO $V_{pc} \approx 61.6 \text{ \AA}^3$. Films on STO or LSAT experience a monoclinic distortion, i. e., $\gamma < 90^\circ$, which has been neglected in the calculation of V_{pc} .

SIO on:	Δa (%)	Δb (%)	Δc (%)	Δd_{220} (%)	ΔV_{pc} (%)
GSO	-0.17	+0.17	+0.12	0	0
DSO	+0.17	+0.35	+0.38	+0.25	+0.64
STO	-0.35	+0.17	-0.88	0	-1.29
LSAT	0	+0.53	-0.88	+0.25	-0.48
NGO	-0.17	+0.35	+0.25	+0.12	+0.16

In summary, SIO films on DSO substrates have $Pbnm$ symmetry with the octahedral tilt pattern of $a^-a^+c^+$ as observed in bulk SIO. In oppose to the effect of compressive strain, the resultant tensile strain reduces orthorhombic lattice distortion. SIO thin films are untwinned only if they are grown on orthorhombic substrates. Epitaxial growth on cubic substrate materials results in a twinning of SIO. Furthermore, SIO on STO or LSAT show a monoclinic distortion which is concomitant with a strong reduction or even vanishing of orthorhombic distortion. Due to the limited experimental resolution in lab-based x-ray diffractometers we cannot rule out the presence of small monoclinic distortion in thin films that were grown on orthorhombic substrates. Generally, film strain is found to be rather small indicating a small critical film thickness t_{cr} well below 60 nm for SIO films. Highest quality of thin films was found for the orthorhombic substrates. Our findings are in good agreement with literature [32,33].

B. Electronic transport

For the resistance measurements, shown in Fig. 4, the films were cooled down from $T = 300$ K to $T = 2$ K and heated up again to 300 K. In the figure we have displayed the resistance versus temperature of (110) SIO on GSO, DSO, STO, and NGO for the two orthogonal directions along the substrate edges. As illustrated in Fig. 5 a), the specific resistances on the orthorhombic (cubic) substrates are obtained as follows: R_{1-10} (R_{010}) = U_{21}/I_{34} and R_{001} (R_{100}) = U_{41}/I_{32} . Interestingly, a distinct difference between R_{1-10} and R_{001} up to 25% is observed for SIO on GSO and DSO. This cannot be explainable by considering geometric factors, e. g., different spacing between the electrical contacts or even inhomogeneity in film thicknesses. The larger resistance is observed along the [1-10] direction. For SIO on NGO the resistance anisotropy is much smaller and for the twinned SIO films on STO or LSAT (not shown) even negligible. Such observations strongly suggest that anisotropic resistance is caused by orthorhombic distortion of the SIO films. Band-structure calculations on SIO [11,23] indeed display high sensitivity towards orthorhombic distortion and lattice strain.

Generally, with decreasing T the resistance first decreases, passes through a shallow minimum around 200 K and then increases again, indicating the vicinity to a metal-to-insulator transition (MIT). Note, that cooling and heating curves match perfectly with each other. Nevertheless, the resistance ratio $R(2\text{ K})/R(300\text{ K})$, which is obviously somewhat larger for SIO on GSO and DSO compared to SIO on STO or NGO, is rather small (≤ 2). For SIO on LSAT (not shown) the resistance is nearly temperature independent. The resistivity of the SIO films at 2 K amounts to $\rho \approx 1\text{ m}\Omega\text{cm}$ and likewise indicates, with respect to the Ioffe-Regel criterion [34], electronic transport close to a MIT. The absolute value of ρ is in good agreement with the ones of bulk SIO and SIO films ($t > 3\text{ nm}$) that are reported in literature [13,19,23,24].

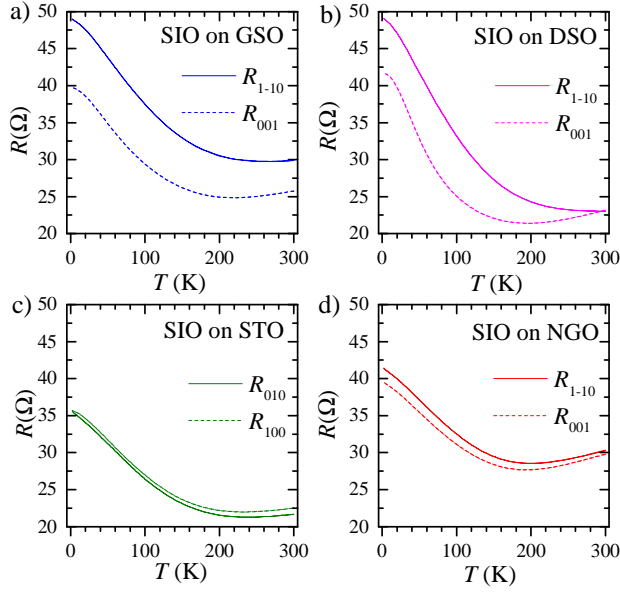


FIG. 4. Resistances R_{1-10} and R_{001} for the two orthogonal in-plane directions of the substrate versus T for SIO on GSO (a), DSO (b), and NGO (d). For definition of the resistances, see Fig. 5. (c) Corresponding resistances R_{010} and R_{100} for SIO on STO. The measurements were carried out during thermal cycling from 300 K to 2 K and from 2 K to 300 K. Note, that cooling and heating curves match each other perfectly.

Fig. 5 b) shows the Hall resistance $R_H = U_{42}/I_{32}$ for SIO on STO at 2 K and 300 K. The linear B -dependence and negative slope of $R_H(B)$ indicate a dominant single-band electron-like transport over the complete T -range.

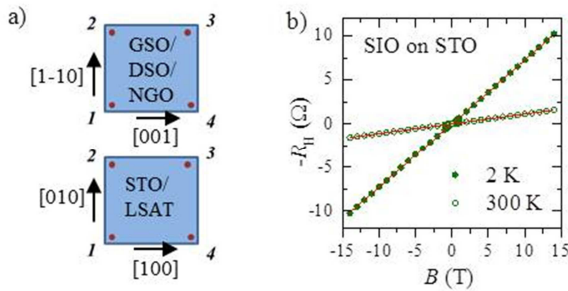


FIG. 5. (a) Schematic of the measurement set-up. Four contacts are bonded to the corners of the 5 mm \times 5 mm square-shaped sample surface. Substrate edges are parallel to the [1-10] and [001] directions for GSO, DSO, and NGO and parallel to the [010] and [100] directions for STO and LSAT. The resistances are measured in four-point in van der Pauw geometry are defined as follows: R_{1-10} and $R_{010} = U_{21}/I_{34}$; R_{001} and $R_{100} = U_{41}/I_{32}$; and $R_H = U_{42}/I_{31}$. (b) Negative Hall resistance R_H (symbols) versus magnetic field B for SIO on STO at $T = 2$ K and 300 K. The solid lines are linear fits to the data.

As demonstrated by ARPES measurements [11], SIO displays a semi-metallic behavior, i. e., electron-like and hole-like pockets close to the Fermi surface. However, effective mass of holes was found to be about 2-6 times larger than the one of electrons, and hence they are less mobile. Moreover, a downshift of hole-like bands is expected for SIO on STO [23], which may justify the assumption of a single electron band to determine charge carrier density. From Fig. 5 b) the deduced electron concentration is $n_e = 9.5 \times 10^{20} \text{ cm}^{-3}$ at 300 K and $n_e = 1.4 \times 10^{20} \text{ cm}^{-3}$ at 2 K. The values of n_e agree well with the ones obtained from ARPES measurements ($4.7 \times 10^{20} \text{ cm}^{-3}$) [11]. The decrease of n_e with decreasing T is likely due to charge trapping by structural defects, which seems to be typical for oxides [35]. The electron mobility increases from $\mu_e = 51 \text{ cm}^2/(\text{Vs})$ at 300 K to $205 \text{ cm}^2/(\text{Vs})$ at 2 K. The electron mean free path $\lambda_m = \hbar/e(3\pi^2 n_e)^{1/3} \mu_e$ reaches 22 nm at 2 K, which is only 1/3 of the entire film thickness. Hence, dimensional constraints may further affect electronic transport.

To analyze the temperature dependence of the anisotropic resistance in more detail, we have plotted the normalized resistance ratio r_N as function of T in Fig. 6. To this end, the resistances $R_{1-10}(T)$, $R_{001}(T)$, $R_{010}(T)$, and $R_{100}(T)$ were first normalized to its room temperature values, $r = R(T)/R(300\text{K})$, and then the ratio r_N between the two orthogonal resistances r_{1-10}/r_{001} and r_{010}/r_{100} were calculated. As already visible in Fig. 4, the anisotropic behavior is significant for SIO on DSO and GSO, very small for SIO on STO and NGO and absent for SIO on LSAT ($r_N(T) \approx 1$). Interestingly, r_N displays pronounced T -dependence and peaks around 100 K for SIO on DSO and GSO. For SIO on STO and NGO, the T -dependence of r_N displays a clear hysteretic behavior during thermal cycling. To underline such hysteretic character we have shown r_N on an enlarged scale in Fig. 6 b). For SIO on STO $r_N(T)$ becomes different below $T = 105$ K for the cooling and heating curves. The resistance hysteresis persists down to 60 K. Below about 60 K, cooling and heating curves coincide again. Remarkably, hysteretic behavior occurs at similar T where STO shows an antiferrodistortive (AFD) cubic-to-tetragonal phase transition [36]. This AFD transition results in an anti-phase rotation of the TiO_6 octahedra along the c -axis, i. e., $(a^0 a^0 c^-)$ according to Glazer's notation.

For SIO on NGO similar hysteretic behavior is observed above 270 K. Interestingly, at 240 K NGO displays structural anomalies alike, which are related to an isosymmetric transition that results in an anomalous hysteretic thermal expansion of the lattice parameters [37-39]. Therefore, the characteristic features at 105 K and 270 K for SIO on STO and NGO, respectively, could be very likely related to structural changes in the substrate material. It is not unusual that the octahedral tilt pattern of perovskite films is affected by the substrate material [40]. However, it is remarkable, that electronic transport in SIO is sensitive to such presumably small structural changes. A reason for that high sensitivity towards structural changes could be probably due to the the narrow bandwidth of the electronic band structure. The octahedral distortion in

combination with the rather large SOC in SIO results in multiple bands depending very sensitively on octahedral tilt and lattice strain [23]. For example, ARPES measurements by Schütz and coworkers [25] revealed that the thickness-dependent metal-insulator transition in SIO films on STO at $t < 3$ unit cells [24] is possibly caused by a suppression of in-plane octahedral rotations which seems to be imposed by the STO substrate. This apparently underscores the high sensitivity of electronic transport with respect to orthorhombic distortions.

The reason for the distinct peak in r_N around 100 K for SIO on DSO and GSO could therefore be related to similar T -dependent structural changes. In bulk SIO, an anomalous thermal expansion of the individual lattice parameters is observed for $T > 100$ K [13]. It is postulated, that SOC alters the nature of the Ir-O bonding, thereby increasing the magnitude of octahedral tilting, which in turn inhibits a transformation to cubic structure at high temperatures. The in-phase and out-of-phase tilt angles amount to about 8.7° and 11.5° , respectively. Usually, the thermal expansion in ABO_3 perovskite oxides can be related to the elongation of B -O bonds and the tilting of the BO_6 octahedra around their three-fold axes [41]. With increasing T , structure goes to higher (cubic) symmetry thereby reducing octahedral rotation. Therefore, thermal expansion is generally expected to be anisotropic [42]. This is also the case for DSO and GSO [43]. The degree of anisotropy of thermal expansion along the individual axes depends on octahedral rotation [43], and should be different for SIO as compared to DSO or GSO, which display significant larger orthorhombic distortions, see Table I. The anisotropic thermal expansion of the orthorhombic substrates likely induces a distinct T -dependence of the octahedral distortion in SIO with respect to the Ir-O bond distances and IrO_6 tilt angles, which again may induce anisotropy in electronic transport. Below 100 K, thermal expansion starts to saturate and lattice parameters are nearly constant [13] leading to a gradual decrease of mismatch between thermal expansion of film and substrate with decreasing T . That might be the reason for the decrease of $r_N(T)$. The exact mechanism involving the degree of rotational correlations between IrO_6 and ScO_6 octahedra and the anisotropic changes in Ir-O bond distances due to the substrate induced anisotropic thermal expansion is certainly complicated and currently beyond the scope of this work. In addition, relaxation of structural mismatch with increasing film thickness may hinder a quantitative analysis. Nevertheless, the influence of the substrate material on the orthorhombic distortion of the SIO films is proven from detailed structural characterization, and very likely the reason for the distinct electronic anisotropy in SIO thin films.

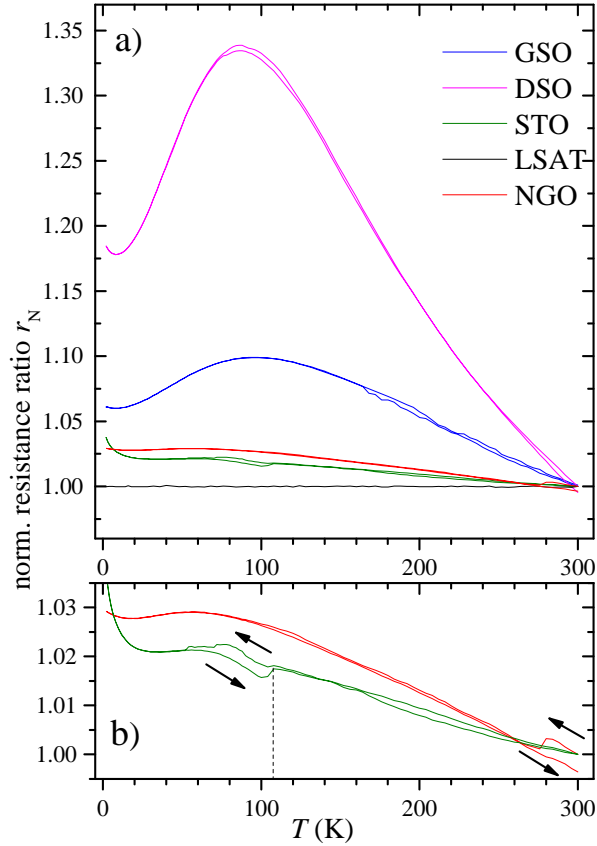


FIG. 6. (a) Normalized resistance ratio r_N , see text, versus T for SIO on GSO, DSO, STO, LSAT and NGO (from top to bottom). First, the samples were cooled down from 300 K to 2 K and then heated up again to 300 K. (b) Enlarged scale of r_N versus T for SIO on STO and NGO. Sample cooling and heating curves are indicated by arrows displaying differences in the range of 70 K - 105 K for SIO on STO and above 270 K for SIO on NGO. The antiferro-distortive transition of STO at 105 K is indicated by the dashed line.

IV. SUMMARY

Perovskite SrIrO_3 (SIO) films were grown epitaxially on various substrate materials by pulsed laser deposition. Films grown on orthorhombic (110) GSO and DSO display bulk-like orthorhombic structure with space group $Pbnm$. The orthorhombic distortion seems to decrease with increasing tensile strain. SIO films deposited on cubic STO and LSAT are twinned and display monoclinic distortion which appears to be increased by increasing compressive strain. Nevertheless, films with a thickness of about 60 nm show quite similar lattice strain which indicates a rather low critical film thickness for pseudomorphic film-growth. Resistance

measurements on the SIO films reveal only weak T -dependence. With decreasing T , the resistance passes through a shallow minimum and then increases slightly. The resistivity of $\rho \approx 1$ m Ω cm at 2 K is well comparable to that of bulk SIO. Hall measurements indicate dominant electron-like transport throughout the temperature range from 2 K – 300 K. At 2 K, the electron concentration and mobility amount to $n_e = 1.4 \times 10^{20}$ cm $^{-3}$ and 205 cm 2 /(Vs). The film resistance for the two orthogonal directions along the GSO and DSO substrate edges is not the same and differs by up to 25% indicating distinct anisotropic behavior. The anisotropy shows pronounced T -dependence with a maximum around 100 K. However, for twinned SIO films grown on STO and LSAT or SIO films on NGO anisotropic behavior is strongly diminished. Small hysteretic behavior of the normalized resistance ratio r_N at $T = 105$ K and 270 K found for SIO on STO and NGO, respectively, indicate that structural changes of the substrate material are likely responsible for the observed anisotropic electronic transport. The rather large anisotropic thermal expansion of DSO and GSO in combination with the untwinned growth of SIO may be responsible for the more pronounced anisotropy of r_N . The substrate induced effects are likely related to constraints with respect to IrO $_6$ octahedral rotations. The strong sensitivity of the electronic transport in SIO films to substrate induced structural changes may be explained in terms of the narrow electron-like bands in SIO caused by SOC and orthorhombic distortion.

ACKNOWLEDGEMENTS

We are grateful to R. Thelen and the Karlsruhe Nano Micro Facility (KNMF) for technical support. DF also acknowledges A. Beck and A. Zaitsev for SEM analysis and K. Sen for fruitful discussions.

V. APPENDIX

A. Orthorhombic distortion in SIO films

With reference to a *doubled pseudo-cubic perovskite cell*, octahedral antiphase rotations of (\vec{a}) and (\vec{b}) produce reflections with $h, k \neq l$ (h, k , and l are odd) e. g., (131), (113), and (311), whereas in-phase rotations (\vec{c}^+) produces reflections with $h \neq k$ (h and k are odd, and l is even), e. g., (130) or (310) [44]. Due to the generally low intensity of such reflections, lab-based x-ray diffraction instruments are less suitable for these studies and experiments with synchrotron radiation are preferred. However, the high crystalline quality of the films allowed us to successfully verify such reflections for the SIO films. Figure 7 shows $2\theta/\omega$ scans on such pseudo-cubic (*single pseudo-cubic perovskite cell*) half-integer reflections of SIO on DSO. The pseudo-cubic a^* , b^* , and c^* -axis were chosen parallel to the orthorhombic [001], [1-10], and [110] directions, respectively. With respect to the orthorhombic symmetry group and octahedral tilt

pattern, only specific half-integer reflections are observed. In contrast, the corresponding pseudo-cubic integer film and substrate reflections are all symmetry-allowed (not shown here). Observed half-integer reflections document $a^+b^-c^-$ tilt-pattern for both SIO and DSO, consistent with $Pbnm$ (62) symmetry and $a^-b^+c^+$ if a^* , b^* , and c^* -axis were chosen parallel to the orthorhombic [110], [1-10], and [001] directions, respectively.

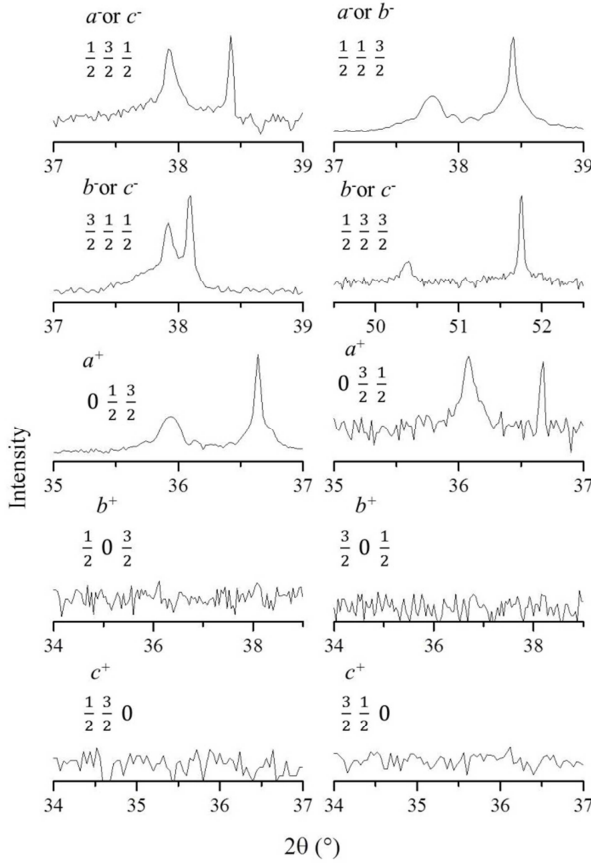


FIG. 7. $2\theta/\omega$ scans on pseudo-cubic half-integer reflections of SrIrO_3 film on DyScO_3 substrate. The pseudo-cubic a^* , b^* , and c^* -axis were chosen parallel to the orthorhombic [001], [1-10], and [110] directions, respectively. The intensity is given on a logarithmic scale. The measurements were carried out in symmetric diffraction conditions. With respect to the octahedral tilt pattern, i. e., in-phase rotation (+) or out-of-phase rotation (-) around a^* , b^* , or c^* -rotation axis - only specific half-integer reflections (as indicated) should be observed. In contrast, the corresponding pseudo-cubic integer film and substrate reflections are all symmetry-allowed and observed (not shown here). The 130, 310, $1/2$ $3/2$ 0 and $3/2$ $1/2$ 0 were measured in grazing incidence geometry. The film reflection appears always to the left side of the substrate reflection. Observed half-integer reflections document $a^+b^-c^-$ tilt-pattern for both SIO and DSO, consistent with $Pbnm$ (62) symmetry.

The epitaxial growth of SIO on cubic substrates such as STO or LSAT is expected to result in twinned films because of the four-fold in-plane symmetry. We likewise carried out $2\theta/\omega$ scans on pseudo-cubic half-integer reflections of SrIrO_3 to verify twinned growth of SIO on these substrates. In Fig. 8, we have shown half-integer reflections of SIO with respect to the pseudo-cubic perovskite cell (see above). The observed half-integer film reflections are only consistent

with the presence of two domains displaying an $a^+b^-c^-$ and $b^-a^+c^-$ tilt-pattern, respectively, which means an in-plane twinning of SIO. The individual tilt pattern is the same as that of bulk SrIrO_3 .

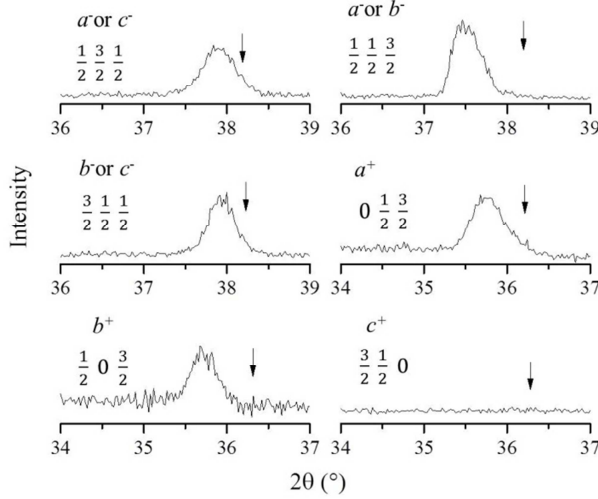


FIG. 8. $2\theta/\omega$ scans on pseudo-cubic half-integer reflections of SrIrO_3 film on SrTiO_3 substrate. The pseudo-cubic a^* , b^* , and c^* -axis were chosen parallel to the orthorhombic $[001]$, $[1-10]$, and $[110]$ directions, respectively. The intensity is given on a linear scale. Maximum peak intensity is well comparable between all the reflections. In contrast to the integer pseudo cubic reflections, which are all observed for both, film and substrate (not shown here), half-integer reflections are only visible for SrIrO_3 and not for cubic SrTiO_3 , which would appear, as indicated by the arrow, to the right of the film reflection. With respect to the orthorhombic symmetry group and octahedral tilt pattern, i. e., in-phase rotation (+) or out-of-phase rotation (-) around a^* , b^* , or c^* -rotation axis - only specific half-integer reflections are observed. Observed half-integer reflections are only consistent with the presence of two domains displaying an $a^+b^-c^-$ and $b^-a^+c^-$ tilt-pattern, i. e., an in-plane twinning of SrIrO_3 . The individual tilt pattern is the same as that of bulk SrIrO_3 .

B. Epitaxial strain in SIO films

To study epitaxial strain and lattice relaxation in more detail, we carried out reciprocal lattice mapping on asymmetric reflections, which allows us to analyze intensity distribution along the in- and out-of-plane direction of the substrate materials. In Fig. 9 we have shown exemplarily reciprocal space maps of the SIO films grown on DSO, STO, and NGO. Since the strain-state of the SIO films does not differ so much (see Table IV), an increasing strain relaxation is expected with increasing lattice mismatch Δ if a pseudomorphic growth is assumed at the beginning of the growth process. That trend is indeed observed in Fig. 9. Small lattice compression of SIO on DSO results in rather negligible lattice relaxation. Therefore, the (332) film peak displays symmetric and sharp intensity distribution with respect to the in-plane direction. For SIO on STO

the lattice spacing difference Δ is larger, hence leading to a stronger smearing-out of the (332) SIO peak intensity towards the peak position of bulk SIO. For SIO on NGO the lattice mismatch is largest amounting to $\Delta = -2.52\%$. Such a high lattice mismatch usually generates very rapid lattice relaxation, i. e., t_{cr} is very small. Therefore, most part of the scattered intensity originates from nearly fully relaxed film material leading again to a rather symmetric intensity distribution. The strong lattice relaxation is also very likely the reason for the increased surface roughness of SIO on NGO, see Table II. Strain relaxation usually increases the mosaic spread of the crystal structure alike, resulting in an additional decrease of peak intensity. This trend can also be well observed in Fig. 9, where the maximum peak intensity of the (332) SIO reflection clearly decreases from left (SIO on DSO) to the right (SIO on NGO).

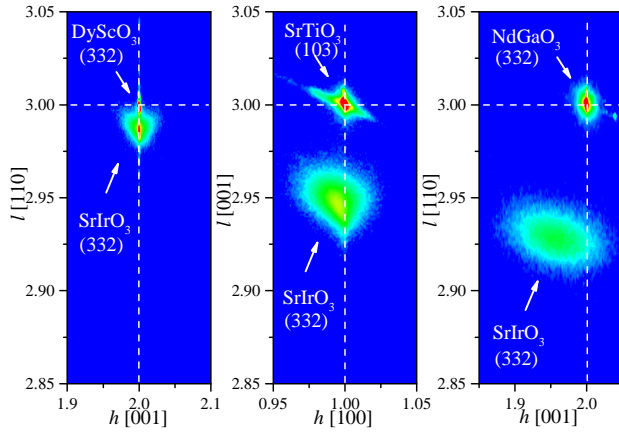


FIG. 9. Contour plots displaying reciprocal space maps of SrIrO₃ thin films grown on (110) DyScO₃ (left), (001) SrTiO₃ (middle), and (110) NdGaO₃ (right). The maps are recorded in the vicinity of the (332) SrIrO₃ reflection. The scattered intensity is given on a logarithmic scale and plotted as a function of the scattering vector q expressed in noninteger Miller indices h, k , and l of the substrate reflection, referring to the azimuth reference [001] ([100]) and the surface normal [110] ([001]) for DyScO₃ and NdGaO₃ (SrTiO₃). Lattice reflections are indicated. In-plane and out-of-plane reciprocal lattice spacing of the substrate reflection are marked by dashed lines.

References:

- [1] G. Cao and L. D. Long, *Frontiers of 4d- and 5d Transition Metal oxides*, World Singapore (2013).
- [2] J. P. Glancy, N. Chen, C. Y. Kim, W. F. Chen, K. W. Plumb, B. C. Jeon, T. W. Noh, Y. J. Kim, *Phys. Rev. B* 86, 195131 (2012).

- [3] D. Pesin and L. Balents, *Nat. Phys.* 6, 376 (2010).
- [4] X. Zhang, H. Zhang, J. Wang, C. Felser, and S. C. Zhang, *Science* 335, 1464 (2012).
- [5] D. Xiao, W. Zhu, Y. Ran, N. Nagaosa, and S. Okamoto, *Nat. Commun.* 2, 596 (2011).
- [6] X. Wan, A. Vishwanath, and S. Y. Savrasov, *Phys. Rev. Lett.* 108, 146601 (2012).
- [7] A. Rüegg, and G. A. Fiete, *Phys. Rev. Lett.* 108, 046401 (2012).
- [8] S. J. Moon, H. Jin, K. W. Kim, W. S. Choi, Y. S. Lee, J. Yu, G. Cao, A. Sumi, H. Funakubo, C. Bernhard, T. W. Noh, *Phys. Rev. Lett.* 101, 226402 (2008).
- [9] B. J. Kim, H. Ohsumi, T. Komesu, S. Sakai, T. Morita, H. Takagi, T. Arima, *Science* 323, 1329 (2009).
- [10] Z. T. Liu, M. Y. Li, Q. F. Li, J. S. Liu, W. Li, H. F. Yang, Q. Yao, C. C. Fan, X. G. Wan, Z. Wang, D. W. Shen, *Sci. Rep.* 6, 30309 (2015).
- [11] Y. F. Nie, P. D. C. King, C. H. Kim, M. Uchida, H. I. Wei, B. D. Faeth, J. P. Ruf, J. P. C. Ruff, L. Xie, X. Pan, C. J. Fennie, D. G. Schlom, and K. M. Shen, *Phys. Rev. Lett.* 114, 016401 (2015).
- [12] A. M. Glazer, *Acta Cryst.* B28, 3384 (1972).
- [13] P. E. R. Blanchard, E. Reynolds, B. J. Kennedy, J. A. Kimpton, M. Avdeev, and A. A. Belik, *Phys. Rev. B* 89, 214106 (2014).
- [14] J. M. Longo, J. A. Kafalas, R. J. Arnott, *J. Solid State Chem.* 3, 174 (1971).
- [15] J. G. Zhao, L. X. Yang, Y. Yu, F. Y. Li, R. C. Yu, Z. Fang, L. C. Chen, C. Q. Jin, *J. Appl. Phys.* 103, 103706 (2008).
- [16] Y.X. Liu, H. Masumoto, T. Goto, *Mater. Trans.* 46, 100 (2005).
- [17] Y.K. Kim, A. Sumi, K. Takahashi, S. Yokoyama, S. Ito, T. Watanabe, K. Akiyama, S. Kaneko, K. Saito, H. Funakubo, *Jpn. J. Appl. Phys.* 45, L36 (2005).
- [18] S.Y. Jang, H. Kim, S.J. Moon, W.S. Choi, B.C. Jeon, J. Yu, T.W. Noh, *J. Phys. Condens. Matter* 22, 485602 (2010).
- [19] A. Biswas, K.-S. Kim, Y.H. Jeong, *J. Appl. Phys.* 116, 213704 (2014).
- [20] D. J. Groenendijk, N. Manca, G. Mattoni, L. Kootstra, S. Gariglio, Y. Huang, E. van Heumen, and A. D. Caviglia, *Appl. Phys. Lett.* 109, 041906 (2016).
- [21] J. M. Carter, V. V. Shankar, M. A. Zeb, and H. Y. Kee, *Phys. Rev. B* 85, 115105 (2012).

- [22] J. L. Lado, V. Pardo, and D. Baldomir, Phys. Rev. B 88, 155119 (2013).
- [23] L. Zhang, Q. Liang, Y. Xiong, B. Zhang, L. Gao, H. Li, Y. B. Chen, J. Zhou, S.-T. Zhang, Z.-B. Gu, S.-H. Yao, Z. Wang, Y. Lin, Y.-F. Chen, Phys. Rev. B 91, 035110 (2015).
- [24] D. J. Groenendijk, C. Autieri, J. Girovsky, M. Carmen Martinez-Velarte, N. Manca, G. Mattoni, A. M. R. V. L. Monteiro, N. Gauquelin, J. Verbeeck, A. F. Otte, M. Gabay, S. Picozzi, and A. D. Caviglia, Phys. Rev. Lett. 119, 256403 (2017).
- [25] P. Schütz, D. Di Sante, L. Dudy, J. Gabel, M. Stübinger, M. Kamp, Y. Huang, M. Capone, M. A. Husanu, V. N. Strocov, G. Sangiovanni, M. Sing, and R. Claesson, Phys. Rev. Lett. 119, 256404 (2017).
- [26] K. Nishio, H. Y. Hwang, and Y. Hikita, APL Mater. 4, 036102 (2016).
- [27] S. S. A. Seo, J. Nichols, J. Hwang, J. Terzic, J. H. Gruenewald, M. Souri, J. Thompson, J. G. Connell, and G. Cao, Appl. Phys. Lett. 109, 201901 (2016).
- [28] L.R. Doolittle, Nucl. Inst. Meth. **B9**, 344 (1985).
- [29] H. C. Montgomery, J. Appl. Phys. 42, 2971 (1971).
- [30] P. Walmsley and I. R. Fisher, Rev. Sci. Instrum. 88, 043901 (2017).
- [31] U. Pietsch, V. Holý, and T. Baumbach, *High-Resolution X-ray Scattering: From Thin Films to Nanostructures*, 2nd ed. New York: Springer (2004).
- [32] J. Liu, D. Kriegner, L. Horak, D. Puggioni, C. Rayan Serrao, R. Chen, D. Yi, C. Frontera, V. Holy, A. Vishwanath, J. M. Rondinelli, X. Marti, R. Ramesh, Phys. Rev. B 93, 085118 (2016).
- [33] L. Horák, D. Kriegner, J. Liu, C. Frontera, X. Marti, and V. Holý, J. Appl. Cryst. 50, 385 (2017).
- [34] A. F. Ioffe and A. R. Regel, Prog. Semicond. 4, 237 (1960).
- [35] D. Fuchs, A. Sleem, R. Schäfer, A. G. Zaitsev, M. Meffert, D. Gerthsen, R. Schneider, and H. v. Löhneysen, Phys. Rev. B 92, 155313 (2015).
- [36] P. A. Fleury, J. F. Scott, and J. M. Worlock, Phys. Rev. Lett. 21, 16 (1968).
- [37] D. I. Savvitskii, S. B. Ubizskii, A. O. Matkovskii, A. Suchocki, U. Bismayer, V. M. Pashkov, V. N. Borisov, A. N. Alexandrovskii, and A. V. Soldatov, Phase Transitions, 70, 57 (1999).
- [38] U. Bismayer, M. Zhang, L.A. Croat, E. K. H. Salje, H.-W. Meyer, Phase Transitions 68 (3), 545 (1999).

- [39] L. Vasylechko, L. Akselrud, W. Morgenroth, U. Bismayer, A. Matkovskii, D. Savytskii, J. Alloys Comp. 297, 46 (2000).
- [40] R. Aso, D. Kan, Y. Fujiyoshi, Y. Shimakawa, and H. Kurata, Crystal Growth & Design, 14 (12), 6478 (2014).
- [41]Y. Zhao and D. J. Weidner, Phys. Chem. Miner. 18, 294 (1991).
- [42] H. D. Megaw, Mater. Res. Bull. 6, 1007 (1971).
- [43] M. D. Biegalski, J. H. Haeni, S. Trolier-McKinstry, and D. G. Schlom, J. Mater. Res. 20, 952 (2005).
- [44] A. M. Glazer, Acta Cryst. A31, 756 (1975).